Universiteit Leiden
The Netherlands

High-contrast imaging polarimetry of exoplanets and circumstellar disks

Holstein, R.G. van

Citation

Holstein, R. G. van. (2021, October 13). *High-contrast imaging polarimetry of exoplanets and circumstellar disks*. Retrieved from https://hdl.handle.net/1887/3217115

Version:	Publisher's Version
License:	Licence agreement concerning inclusion of doctoral thesis in the Institutional Repository of the University of Leiden
Downloaded from:	https://hdl.handle.net/1887/3217115

Note: To cite this publication please use the final published version (if applicable).

1 Introduction

In astronomy, the light originating from astrophysical objects is often only studied in terms of its intensity as a function of wavelength through photometry and spectroscopy. However, light is a transverse, electromagnetic wave and therefore has polarization: The electric (and magnetic) fields of the light oscillate or rotate in a certain direction. By performing polarimetry, that is, by measuring the polarization state of the light, we can retrieve much more information about the observed astrophysical objects. Indeed, spectropolarimetry measures the intensity of the light as a function of wavelength and polarization state, and can therefore determine the full information content of the electromagnetic radiation.

Polarimetry is a particularly powerful tool for the direct imaging of circumstellar disks and substellar companions, that is, exoplanets and brown dwarf companions, at near-infrared (NIR) and visible wavelengths. Direct imaging spatially separates the light from the object of interest and the light from the central star. However, this is a very challenging task because circumstellar disks and substellar companions are generally located at angular separations (much) smaller than 1″ from their parent stars and are orders of magnitude fainter than the star. To overcome this challenge, dedicated high-contrast imaging instruments are built that can reach a large contrast very close to the star. Almost all of these instruments operate from the ground and several have polarimetric capabilities.

The first reason that high-contrast imagers employ polarimetric modes is to reach the contrast required to image circumstellar disks and companions. The direct light from the central star is generally unpolarized: The light is a mixture of equal amounts of all possible polarization states. As this starlight scatters off dust grains in the circumstellar disk or off the companion's atmosphere, it becomes linearly polarized. Therefore, when taking an image in linearly polarized light, the direct starlight is strongly suppressed, while the partially polarized light from the circumstellar disk or companion is revealed.

The second reason to perform high-contrast imaging polarimetry is related to characterization; polarimetric images do not only reveal the morphology of circumstellar disks and the architecture of planetary systems, but they also contain information on the physical properties of the scattering particles. Measurements of polarization as a function of wavelength can, for instance, be used to constrain the composition, size, and shape of the dust grains in circumstellar disks and to determine the properties of the atmospheres or surfaces of companions.

The outline of this introductory chapter is as follows. In Sect. 1.1, I discuss the formation and evolution of circumstellar disks and substellar companions and outline what we can learn from polarimetric measurements of these objects. Subsequently, in Sect. 1.2, I describe the components and workings of a high-contrast imaging instrument. In Sect. 1.3, I then outline how polarimetric measurements are taken with a high-contrast imager and describe the instrumental effects that can reduce the performance of the instrument. Finally, I give an outline of the thesis in Sect. 1.4 and present an outlook in Sect. 1.5.

1.1 Polarimetry to study circumstellar disks and substellar companions

The formation of circumstellar disks and substellar companions is closely related to the formation of stars. Stars form inside massive clouds of molecular gas and dust that are located in the interstellar medium (Shu et al., 1987; McKee & Ostriker, 2007). Such a molecular cloud is gravitationally unstable; parts of the cloud fragment and collapse under their own gravity. This results in the formation of dense cores that further collapse to form stars (Shu, 1977; Bate, 1998). Because the collapsing core has a net angular momentum, a rotating disk of dust and gas forms around the forming star from which the star accretes material (Yorke et al., 1993; Nakamoto & Nakagawa, 1994). This disk is called a protoplanetary disk because planets (and brown dwarf companions) are believed to form in this disk (Beckwith & Sargent, 1996; Williams & Cieza, 2011). These substellar companions may form through the coagulation of dust into kilometer-sized planetesimals and the subsequent accretion of planetesimals and gas (Pollack et al., 1996; Chambers, 2004; Bodenheimer et al., 2013), the local collapse of part of the disk due to gravitational instabilities (Cameron, 1978; Boss, 1997; Stamatellos et al., 2007; Kratter et al., 2010), or the direct collapse of a separate core in the molecular cloud (Hennebelle & Chabrier, 2008; Bate, 2009). In all these scenarios the companions are expected to have their own circumsubstellar (accretion) disks (e.g., Stamatellos & Whitworth, 2009; Szulágyi et al., 2017), from which in turn moons may form (Canup & Ward, 2002). As time progresses, the protoplanetary disk disperses due to the formation of companions, accretion onto the star, stellar winds, photoevaporation by ultraviolet radiation, and gravitational interactions with nearby stars (Hollenbach et al., 2000). In some cases, a debris disk remains that consists of second-generation dust produced by the collisions of left-over planetesimals (Wyatt, 2008). Over time, the formed companions cool as they radiate the heat from their formation and continuing contraction (Chabrier et al., 2000; Baraffe et al., 2003), producing a planetary system similar to our own Solar System.

Protoplanetary disks and debris disks are routinely imaged in linearly polarized light with the current high-contrast imaging instruments. These instruments include SPHERE at the Very Large Telescope (see Fig. 1.1; Beuzit et al., 2019), SCExAO at the Subaru Telescope (Jovanovic et al., 2015), and the Gemini Planet Imager (GPI) at the Gemini South Telescope (Macintosh et al., 2014). Whereas GPI (Perrin et al., 2015), the IRDIS subsystem of SPHERE (Dohlen et al., 2008; de Boer et al., 2020; Chapter 2), and the CHARIS subsystem of SCExAO (Groff et al., 2017; Lozi et al., 2020a) perform polarimetric measurements at NIR wavelengths, the ZIMPOL polarimeter of SPHERE (Schmid et al., 2018) operates at visible wavelengths. These instruments principally employ polarimetry as a means to overcome the contrast between the star and the circumstellar disk, which typically is at a disk-to-star contrast of 10^{-2}–10^{-4} in the case of a protoplanetary disk (e.g., Garufi et al., 2020) and at a contrast of 10^{-4}–10^{-6} in the case of a debris disk (e.g., Esposito et al., 2020). After a disk has been detected in polarized light, the measurements are often used to study the extent, orientation, and morphology of the disk. In protoplanetary disks we can observe a wide variety of substructures, such as rings, cavities, gaps, spiral arms, and shadows (see Fig. 1.2, left; e.g., Muto et al., 2012; Quanz et al.,

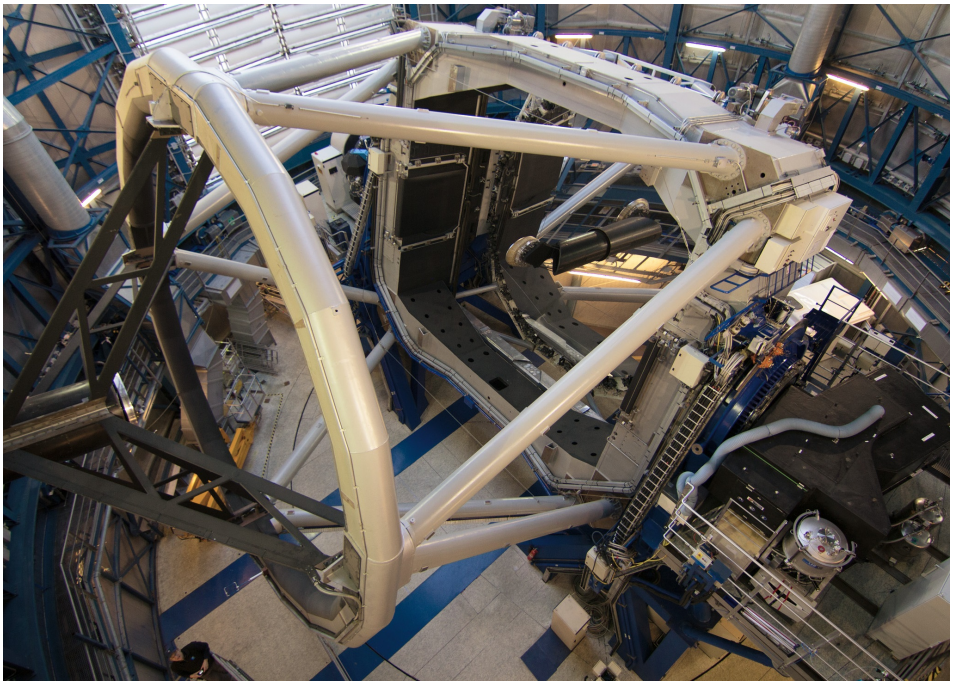

Figure 1.1: Unit Telescope 3 of the Very Large Telescope with SPHERE installed on the Nasmyth platform (bottom right). Image credit: J. H. Girard / ESO.

2013; Benisty et al., 2015; Ginski et al., 2016; Stolker et al., 2016b; de Boer et al., 2016; Benisty et al., 2017; Van Boekel et al., 2017; Pinilla et al., 2018; Garufi et al., 2018), some of which may be caused by companions interacting with the disk (Kley & Nelson, 2012; Dong et al., 2015; Zhu et al., 2015; Dong et al., 2016). The morphology of debris disks is generally simpler and often consists of a single ring (see Fig. 1.2, right; e.g., Engler et al., 2017; Olofsson et al., 2019; Esposito et al., 2020). Linear-polarization measurements are also used to constrain the properties of the dust in the disks by measuring polarized scattering phase functions and performing radiative transfer modeling (e.g., Perrin et al., 2015; Milli et al., 2015; Olofsson et al., 2016; Stolker et al., 2016a; Ginski et al., 2016; Benisty et al., 2017). Measurements of circular polarization could yield additional constraints on the dust properties as well as on scattering asymmetries and magnetic-field geometries (Bastien & Menard, 1990; Gledhill & McCall, 2000), but none of the current high-contrast imagers are designed to measure circular polarization.

Young exoplanets and brown dwarf companions emit the majority of the heat from their formation as NIR radiation. Current high-contrast imaging instruments can directly image these self-luminous companions in NIR total intensity at contrasts of 10^{-2}–10^{-6} (e.g., Bowler, 2016; Nielsen et al., 2019; Langlois et al., 2021). Typically, the companions are studied with photometry and spectroscopy (e.g., Bowler et al., 2014; Bonnefoy et al., 2016; Müller et al., 2018). However, the companions can also be characterized by measuring their NIR linear polarization. This polarization is created as the thermal radiation

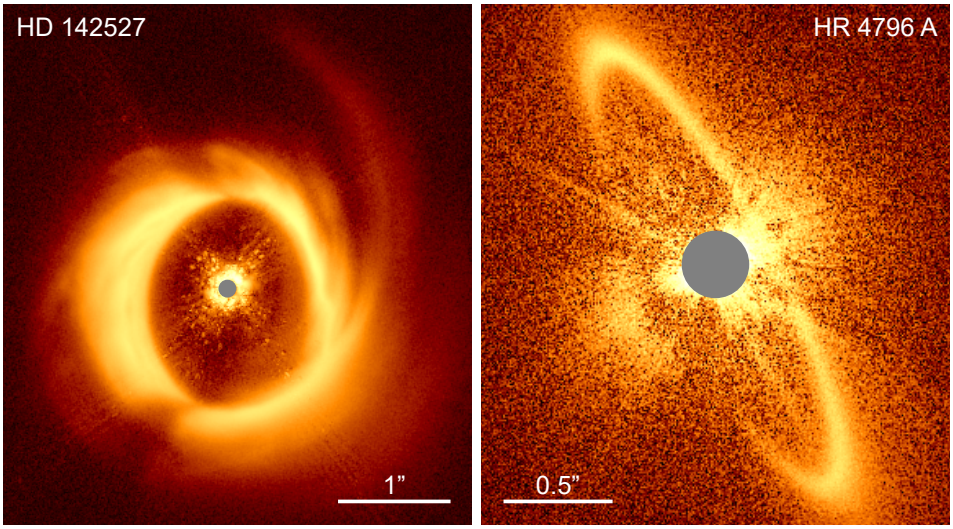

Figure 1.2: Linearly polarized intensity images of the protoplanetary disk of HD 142527 as taken with SPHERE-IRDIS (*left*; Hunziker et al., 2021) and the debris disk of HR 4796 A as taken with SPHERE-ZIMPOL (*right*; Olofsson et al., 2019). Both images are shown on a different logarithmic scale and contain some instrument-induced spurious signal near the center. The gray areas cover the regions where measurements are unreliable.

emanating from within the companion is scattered by dust in the companion's atmosphere (Sengupta & Krishan, 2001). Because the companion is observed as a point source, we only see the polarization integrated over the companion. Whereas for a spherically symmetric companion the integrated signal is zero, a net polarization remains when this symmetry is broken. Examples of these asymmetries are rotation-induced oblateness and an inhomogeneous distribution of atmospheric dust clouds (see Fig. 1.3, left; Sengupta & Marley, 2010; de Kok et al., 2011; Marley & Sengupta, 2011; Stolker et al., 2017). A companion can also be polarized when it has a circumsubstellar disk (see Fig. 1.3, right; Stolker et al., 2017), analogous to how pre-main-sequence stars can be polarized when they host a circumstellar disk (e.g., Rostopchina et al., 1997; Bouvier et al., 1999; Grinin, 2000; Menard et al., 2003). Based on models, the degree of linear polarization due to atmospheric asymmetries and circumsubstellar disks can reach several tenths of a percent, and even up to several percent in favorable cases. The NIR polarization of substellar companions can perhaps be measured with GPI and SPHERE-IRDIS, but attempts to detect these signals with GPI have so far been unsuccessful (Millar-Blanchaer et al., 2015; Jensen-Clem et al., 2016).

Contrary to young companions, most of the flux from evolved, cool exoplanets is reflected, visible starlight. This reflected flux is much smaller than the thermal NIR flux of young companions, with giant exoplanets having contrasts of $\sim 10^{-8}$ (e.g., Hunziker et al., 2020) and rocky exoplanets having contrasts of $\sim 10^{-10}$ (e.g., Traub & Oppenheimer, 2010). However, the reflected flux is expected to be linearly polarized at up to

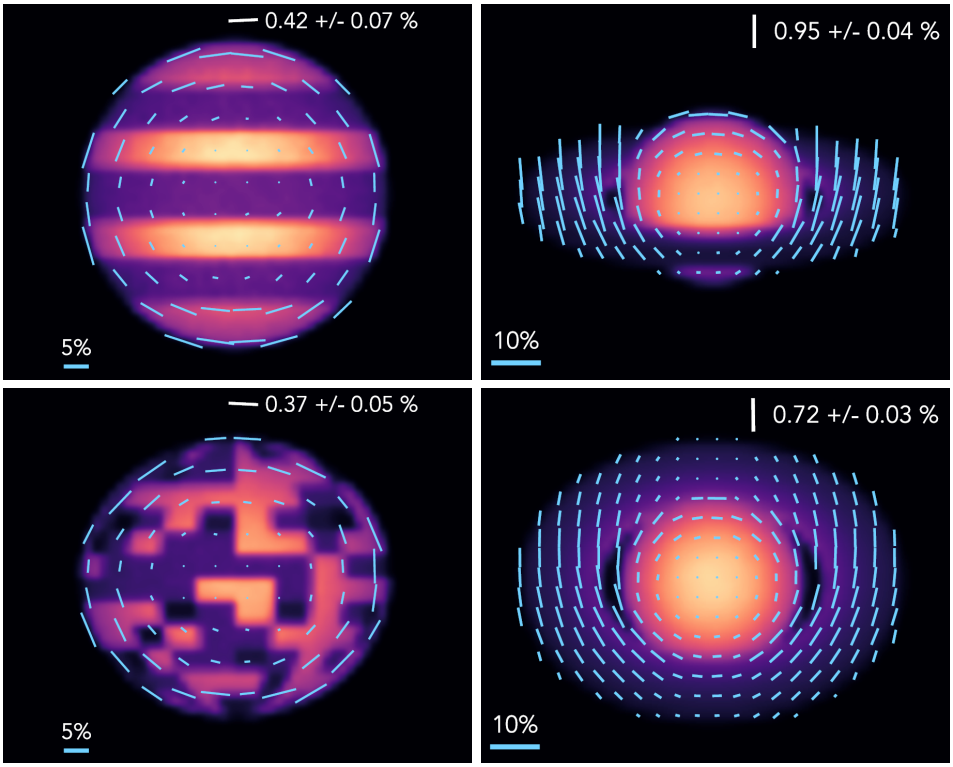

Figure 1.3: Models of the linear polarization of companions from Stolker et al. (2017) showing a companion with banded cloud structure (*top left*), an oblate companion with patchy clouds (*bottom left*), and a companion with a circumsubstellar disk viewed at high inclination (*top right*) as well as low inclination (*bottom right*). The blue lines indicate the local degree and angle of linear polarization. The integrated polarization for each companion is shown in the top right of each panel.

several tens of percent (Stam et al., 2004; Hunziker et al., 2020). Polarimetry is therefore useful to suppress the unpolarized starlight and directly image the planets. In addition, spectropolarimetry at visible wavelengths can be used to characterize these directly imaged exoplanets, at a level beyond that possible with conventional intensity spectroscopy alone. In the case of giant exoplanets, linear spectropolarimetry can be used to constrain the composition and structure of the atmosphere and reveal the presence of atmospheric clouds (Stam et al., 2004; Buenzli & Schmid, 2009). For rocky exoplanets, linear spectropolarimetry can constrain the habitability of the planet by determining the presence of liquid or icy water clouds in the atmosphere (Bailey, 2007; Karalidi et al., 2011, 2012), the type and percentage of cloud cover (Rossi & Stam, 2017), and even the presence of oceans and continents (Stam, 2008; Williams & Gaidos, 2008; Karalidi & Stam, 2012; Trees & Stam, 2019). Circular spectropolarimetry might even reveal the presence of life through the detection of biological homochirality (Sparks et al., 2009; Rossi & Stam,

2018; Patty et al., 2019). Life on Earth largely prefers one of two mirror-image versions of chiral molecules, and this causes the light interacting with chiral biological molecules and structures to become circularly polarized. SPHERE-ZIMPOL is specifically designed to search for the linearly polarized, reflected light of cool, giant exoplanets, but has so far been unsuccessful at detecting them (Hunziker et al., 2020). In the near future, the polarized light of these giant exoplanets could perhaps also be detected with the Nancy Grace Roman Space Telescope (Spergel et al., 2015), although the telescope's polarimetric mode is better suited for the imaging and characterization of circumstellar disks (Bailey et al., 2018; Kasdin et al., 2020). Finally, in the next decade, it should be possible to detect giant and rocky exoplanets in polarized light with ground-based high-contrast imagers such as PCS (or EPICS) at the Extremely Large Telescope (ELT; Kasper et al., 2020) and PSI at the Thirty Meter Telescope (Fitzgerald et al., 2019), as well as with the dedicated polarimetric modes of the proposed space telescopes HabEx (Gaudi et al., 2020) and LUVOIR (LUVOIR Team, 2019).

1.2 High-contrast imaging

Direct imaging of circumstellar disks and substellar companions is challenging because we need to reach extreme contrasts at very small angular separations from the star. Ground-based high-contrast imaging instruments are therefore installed on the largest telescopes and have complex optical systems designed to create near diffraction-limited images and suppress the light from the star. To further suppress the starlight and reach the required contrast, these instruments also employ advanced differential imaging techniques and data-reduction methods.

1.2.1 Components of a high-contrast imager

A schematic of a ground-based high-contrast imaging instrument is shown in Fig. 1.4. For this example, the instrument is located on the Nasmyth platform of a telescope on an alt-azimuth mount, as is the case for SPHERE and SCExAO. The light incident on the telescope is collected by the concave primary mirror and is subsequently refocused by the convex secondary mirror that is suspended at the top of the telescope. The flat tertiary mirror then reflects the light to the Nasmyth platform. When the alt-azimuth telescope mount tracks a target across the sky, the target rotates with the parallactic angle with respect to the telescope pupil, and the telescope rotates with the telescope altitude angle with respect to the Nasmyth platform. To compensate the resulting rotation of the image, the instrument includes an image derotator, which is a rotating assembly of three mirrors (a K-mirror) that can rotate the image to any orientation. The derotator generally has two main operating modes. In field-tracking mode, the derotator keeps the image orientation constant during an observation, allowing for long integrations without smearing of the image. In pupil-tracking mode, the derotator instead keeps the pupil of the telescope fixed, while the target rotates with the parallactic angle around the center of the image. Note that GPI, which is mounted at the Cassegrain focus, does not use a derotator and therefore always observes in pupil-tracking mode.

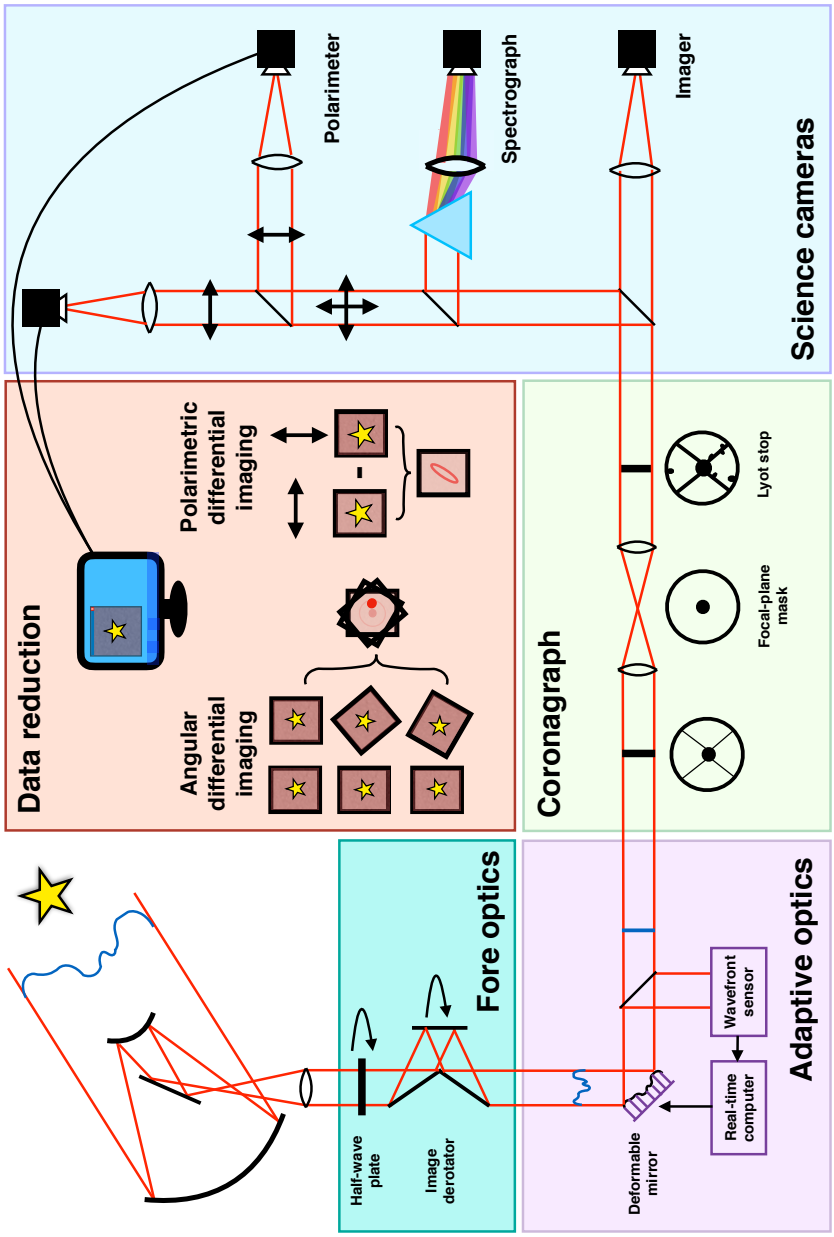

Figure 1.4: Schematic of a ground-based high-contrast imaging instrument installed on a Nasmyth platform, showing the telescope and fore optics, adaptive optics, coronagraphs, science cameras, and data reduction. Image courtesy of David Doelman.

The theoretical angular resolution of the current 8-m class telescopes, as limited by diffraction, is between 12 mas to 80 mas at visible and near-infrared wavelengths. However, for ground-based telescopes the turbulence in the Earth's atmosphere distorts the (initially flat) wavefront of the light arriving from the star (Fried, 1966; Greenwood, 1977). As a result, the angular resolution that these telescopes achieve for typical conditions is much worse, and the full width at half maximum of the point-spread function (PSF) is only on the order of 1″ (see Fig. 1.5, top left). To correct the wavefront distortions, ground-based high-contrast imaging instruments employ adaptive-optics (AO) systems (e.g., Guyon, 2018). These AO systems generally contain a (dichroic) beamsplitter that sends part of the light to a wavefront sensor that measures the distortion in the wavefront (see Fig. 1.4). These measurements are then sent to a computer that calculates the necessary wavefront correction in real-time and controls a deformable mirror that flattens the wavefront. After the AO correction, the PSF is nearly diffraction-limited (see Fig. 1.5, top right).

To overcome the large contrast between the star and the object of interest close to the star, high-contrast imagers use coronagraphs. Coronagraphs are optical devices that remove starlight due to diffraction at the telescope aperture. Many types of coronagraphs act as angular filters: The on-axis transmission is very low whereas the off-axis transmission is high. The simplest coronagraph is the classical Lyot coronagraph invented to study the solar corona outside of eclipses (Lyot, 1939). The Lyot coronagraph consists of a focal-plane mask that blocks the central peak of the PSF of the star and an aperture mask in the subsequent pupil plane, called the Lyot stop, that blocks the light that is diffracted by the focal-plane mask (see Fig. 1.4). Over the years, a wide range of more advanced coronagraphs have been developed (e.g., Guyon et al., 2006; Mawet et al., 2012; Ruane et al., 2018). After the light passes the coronagraph, the starlight is significantly suppressed, thereby enhancing the contrast close to the star. However, remaining wavefront aberrations create speckles in the PSF (see Fig. 1.5, center left) that limit the contrast.

After passing the coronagraph, the light is captured by the detector(s) of one or more science cameras (see Fig. 1.4). The simplest science camera is an imager that use a range of broadband and narrowband filters. SPHERE-IRDIS and SPHERE-ZIMPOL have such imaging modes (Dohlen et al., 2008; Schmid et al., 2018). Another type of science camera is the spectrograph. SCExAO-CHARIS and GPI both employ an integral-field spectrograph (IFS) that uses a lenslet array and a dispersive element to create low-resolution spectra over a 2D field of view (Groff et al., 2017; Larkin et al., 2014). SPHERE-IRDIS also has a long-slit spectroscopy mode that creates a spectrum of the light passing through a slit placed across the field of view (Vigan et al., 2008). Finally, the linear polarization state of the light can be measured with a polarimeter. As discussed in Sect. 1.1, SPHERE-IRDIS, SPHERE-ZIMPOL, SCExAO-CHARIS, and GPI all have linear polarimetric modes. SCExAO-CHARIS combines its polarimetric capability with its IFS to enable low-resolution spectropolarimetry (Lozi et al., 2020a). All these high-contrast imaging polarimeters are of the dual-beam type where a polarizing beamsplitter, or a combination of a nonpolarizing beamsplitter and polarizers, is used to split the beam of light incident on the science camera into two beams with orthogonal linear polarization states (e.g., Snik & Keller, 2013). These beams then fall on the detector(s) to simultaneously create two images. Images in polarized light are then computed as the difference of these

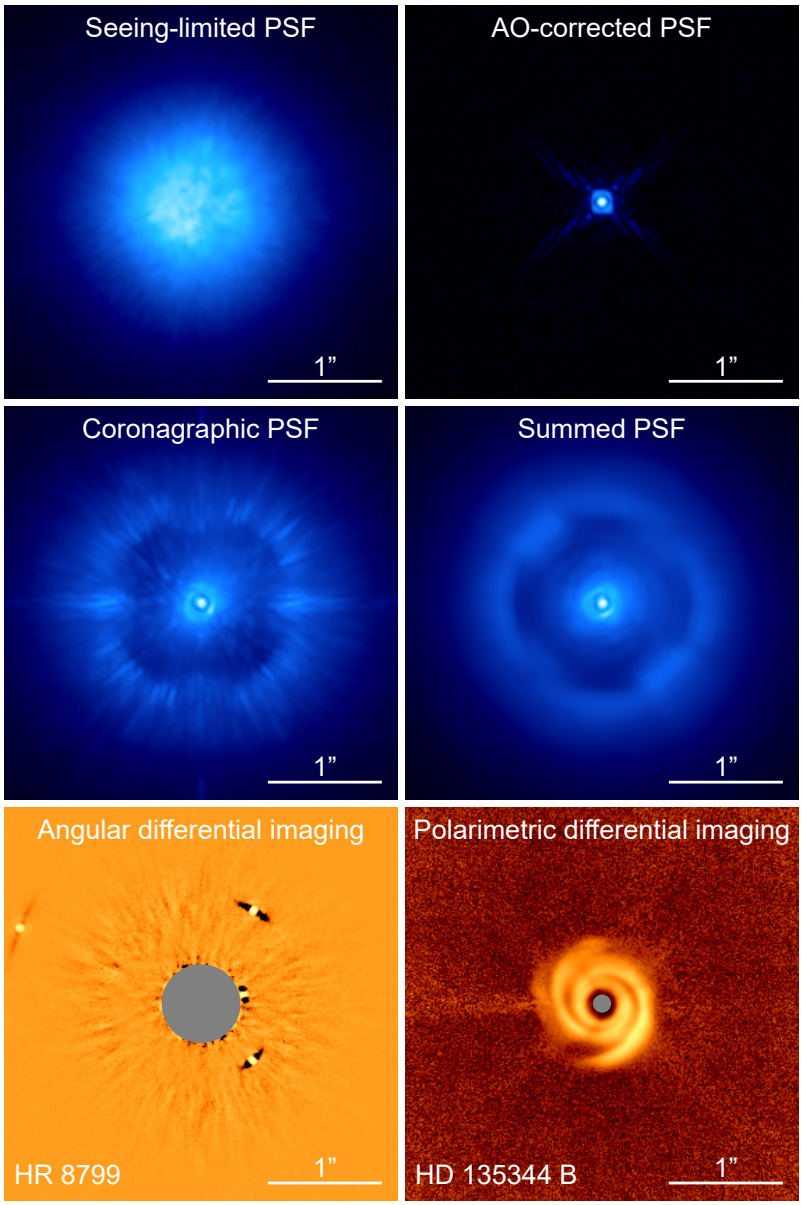

Figure 1.5: Gallery of SPHERE-IRDIS images of the seeing-limited PSF, the AO-corrected PSF, the coronagraphic PSF, the PSF summed over an observation sequence, the total intensity of the four planets of HR 8799 after applying ADI with PCA (Chapter 4), and the linearly polarized intensity of the protoplanetary disk of HD 135344 B after applying PDI (Stolker et al., 2016b). All panels are shown on a (different) logarithmic scale. The angular scales of all panels are the same. The gray areas in the bottom panels cover the regions where measurements are unreliable.

two images. A rotatable half-wave plate (HWP) located at the beginning of the optical path (see Fig. 1.4) is used as a polarization modulator and selects the linear polarization state to be measured.

1.2.2 Differential imaging techniques

When summing the frames of an observation sequence, significant stellar signal remains that can hide substellar companions or a circumstellar disk (see Fig. 1.5, center right). To remove the stellar PSF and further enhance the contrast, a variety of differential imaging techniques, which are applied during the data reduction, have been developed. The two most successful techniques for ground-based high-contrast imaging are angular differential imaging (ADI) and polarimetric differential imaging (PDI).

ADI (see Fig. 1.4; Marois et al., 2006) is primarily used to detect substellar companions in total intensity. To apply ADI, observations are performed in pupil-tracking mode. This way, the stellar PSF and its speckle pattern are stationary on the detector during the observations, while any point sources rotate with the parallactic angle around the center of the image. A model of the stellar PSF is then created during the data reduction by computing the median over all frames. Because any point sources around the star will be at a different position in each frame, their contribution to the PSF model will be very small. We then subtract the PSF model from all frames, derotate these PSF-subtracted frames (i.e., align them such that north is up), and sum the resulting frames. This procedure yields a final image in which the stellar PSF is almost completely removed and any sufficiently bright point sources are visible. To optimize the starlight suppression, the PSF model is often constructed using more advanced algorithms such as principal component analysis (PCA; Soummer et al., 2012; Amara & Quanz, 2012) instead of simply computing the median over the frames (see Fig. 1.5, bottom left).

PDI (see Fig. 1.4; Kuhn et al., 2001) is primarily used to detect the polarized, scattered light from circumstellar disks. In PDI, we use a dual-beam polarimeter to simultaneously take two images of orthogonal polarization states and compute the difference of these two images. Because stars are generally unpolarized (or at least have a very low degree of polarization) and the images are taken under the exact same atmospheric conditions, the intensity of the stellar PSF is virtually the same in both images, and therefore the stellar PSF is strongly suppressed in the difference. At the same time, the polarized light originating from a circumstellar disk has different intensities in the two images and is therefore visible in the difference (see Fig. 1.5, bottom right). With PDI we can thus attain large gains in contrast, but only for objects that are polarized.

1.3 Polarimetry

The performance of high-contrast imaging polarimeters is predominantly limited by two effects (e.g., Keller, 2002; Snik & Keller, 2013). Spurious signals and other noise in the images reduce the polarimetric sensitivity, that is, the noise level in the images above which polarization signals can be detected. In addition, telescope- and instrument-induced changes to the polarization state of light affect the polarimetric accuracy, that is, the dif-

ference between the measured polarization state and the polarization state incident on the telescope. To detect and accurately characterize substellar companions and circumstellar disks, high-contrast imaging polarimeters need to have both a high polarimetric sensitivity and a high polarimetric accuracy.

1.3.1 Description of polarized light

The polarization state of light can be described by the Stokes vector $\boldsymbol{S}$ (e.g., Tinbergen, 2005):

$$\boldsymbol{S} = \begin{bmatrix} I \\ Q \\ U \\ V \end{bmatrix}, \tag{1.1}$$

where I is the total intensity of the light, Q and U describe linearly polarized light, and V describes circularly polarized light. On the sky, positive Q is generally aligned with the north-south direction, and negative Q with the east-west direction (e.g., Hamaker & Bregman, 1996; Snik & Keller, 2013). Positive and negative U are oriented at 45° counterclockwise and clockwise, respectively, from positive Q, and positive and negative V describe circular polarizations of opposite handedness. From these Stokes parameters we can calculate the linearly polarized intensity PI_{L}, the degree of linear polarization P, and the angle of linear polarization χ as:

$$PI_{\mathrm{L}} = \sqrt{Q^2 + U^2}, \tag{1.2}$$

$$P = \frac{PI_{\mathrm{L}}}{I} = \frac{\sqrt{Q^2 + U^2}}{I}, \tag{1.3}$$

$$\chi = \frac{1}{2} \arctan\left(\frac{U}{Q}\right). \tag{1.4}$$

1.3.2 Polarization measurements with the double difference

Using a dual-beam polarimeter, images of Q and U can, in principle, be obtained by taking measurements with the HWP at angles (with respect to some defined reference direction) equal to 0° and 22.5°, respectively, and then computing the difference of the two images of the orthogonal linear polarization states, as described for PDI in Sect. 1.2.2. However, the stellar PSF is not perfectly removed when computing the difference. This is primarily due to the diattenuation of the optical components within the instrument, which causes the two orthogonal linear polarization states to be reflected and transmitted with different efficiencies (Canovas et al., 2011). In addition the two beams of light experience different wavefront aberrations, and the images they create contain different flat-field errors. These differential effects create spurious signals and noise that negatively affect the polarimetric sensitivity, especially at small angular separations from the star, close to the edge of the focal-plane mask of the coronagraph.

To suppress the differential effects and greatly increase the sensitivity, two additional measurements are performed. A total of four measurements are taken with HWP angles equal to 0°, 45°, 22.5°, and 67.5°. At each HWP angle, we compute the difference of the two images and denote the results as Q^+, Q^-, U^+, and U^-, respectively. We then compute the images of Q and U from the so-called double difference (e.g., Bagnulo et al., 2009):

$$Q = \frac{1}{2}\left(Q^+ - Q^-\right), \tag{1.5}$$

$$U = \frac{1}{2}\left(U^+ - U^-\right). \tag{1.6}$$

After computing the double difference, the differential effects are significantly reduced. Some spurious signals and noise still remain because the two measurements used to compute the double difference are not taken simultaneously and therefore experience (slightly) different atmospheric conditions and AO correction. As a result of these variations, the effect of the diattenuation of the components downstream of the HWP is not completely removed.

1.3.3 Instrumental polarization effects and polarization aberrations

After applying the double difference, the measurements are still affected by instrumental polarization effects, which consist of instrumental polarization (IP) and polarization crosstalk. IP is the polarization signal produced by the instrument or telescope and can make unpolarized sources appear to be polarized. It results from the diattenuation of the optical components located upstream of the HWP, which in Fig. 1.4 is the telescope. This diattenuation is not removed in the double difference and creates a halo of polarized light in the Q- and U-images. Crosstalk is the telescope- or instrument-induced mixing of polarization states. It is caused by the retardance of the optical components, which induces a relative phase shift between the two orthogonal linear polarization states. Crosstalk causes an offset of the measured angle of linear polarization and can lead to significant losses of polarization signal. If uncorrected for, the instrumental polarization effects can strongly decrease the polarimetric accuracy of the measurements. Fortunately, the instrumental polarization effects of high-contrast imaging polarimeters can be corrected for through theoretical modeling (e.g., Witzel et al., 2011), or more accurately, with calibration measurements (e.g., de Boer et al., 2014; Wiktorowicz et al., 2014; Millar-Blanchaer et al., 2016).

The coronagraphic performance and achievable contrast of the most sensitive high-contrast imagers are furthermore limited by polarization aberrations (e.g., Chipman, 1989; McGuire & Chipman, 1990; Sanchez Almeida & Martinez Pillet, 1992; McGuire & Chipman, 1994a,b; Breckinridge et al., 2015). Polarization aberrations are minute, polarization-dependent variations of the amplitude and phase of the electromagnetic field across a beam of light that result in polarization structures in the PSF. The diattenuation and retardance, which cause the instrumental polarization effects, can be considered to be zeroth-order polarization aberrations. The first-order polarization aberrations are polarization-dependent wavefront tilts induced by oblique reflection and are connected

to subwavelength-sized shifts of the PSF. Higher-order aberrations, such as polarization-dependent astigmatism, are produced by curved mirrors such as the primary and secondary mirrors of a telescope (see Fig. 1.4). Recently, it was found that the polarimetric speckle suppression of SPHERE-ZIMPOL at small angular separations is limited by reflection-induced beam shifts (Schmid et al., 2018). It is therefore becoming clear that polarization aberrations need to be fully controlled and mitigated for any instrument aiming to achieve the polarimetric sensitivity to detect exoplanets in reflected, polarized light.

1.4 Outline of this thesis

The goals of this thesis are to improve the polarimetric sensitivity, accuracy, and capabilities of high-contrast imaging polarimeters for the detection and characterization of substellar companions and circumstellar disks. In addition, this thesis presents the first direct detections of linear polarization from self-luminous substellar companions. The focus of this thesis is mostly on ground-based high-contrast imaging, in particular with SPHERE-IRDIS. The thesis covers many aspects of high-contrast imaging polarimetry, ranging from theoretical work, calibrations, and the development of new observing techniques to actual scientific polarimetric measurements and astrophysical interpretation.

Chapter 2: Calibration of the instrumental polarization effects of SPHERE-IRDIS

In Chapter 2 we characterize the instrumental polarization effects of SPHERE-IRDIS using measurements with SPHERE's internal light source and observations of unpolarized stars. We find that the IP is almost exclusively produced by the telescope and SPHERE's first mirror, whereas the crosstalk primarily originates from the image derotator. At some orientations, the derotator causes severe loss of signal in the H- and K_s-band as it converts incident linearly polarized light into circularly polarized light. We develop a data-reduction method that corrects the instrumental polarization effects and apply it to observations of a circumstellar disk. With our correction method we reach a polarimetric accuracy of $\lesssim 0.1\%$ in the degree of linear polarization. We have incorporated the correction method in a highly automated end-to-end data-reduction pipeline called `IRDAP`, which is publicly available.

IRDAP enables us to accurately measure the linearly polarized intensity and angle of linear polarization and is currently the go-to pipeline for IRDIS polarimetric data. It is fundamental to the first detections of linear polarization from substellar companions as presented in Chapter 5 and laid the foundation for many scientific publications on circumstellar disks. Among these publications are the detection of non-azimuthal polarization, indicative of multiple scattering, in the circumstellar disk of T Cha (Pohl et al., 2017); the first detection of polarization from a low-mass stellar companion, CS Cha B (Ginski et al., 2018); the detection of the inner circumstellar disk of PDS 70 (Keppler et al., 2018); the discovery of an outer belt and spiral arm in the TWA 7 debris disk (Olofsson et al., 2018); the accurate tracing of the movement of the spiral arms in the MWC 758 disk, which indicates the spiral arms are driven by an unseen planetary perturber (Ren et al., 2020); and many others (Canovas et al., 2018; Bhowmik et al., 2019; Garufi et al.,

2020; Muro-Arena et al., 2020; Boccaletti et al., 2020a; Keppler et al., 2020; Ménard et al., 2020; Kennedy et al., 2020; Rigliaco et al., 2020; Kraus et al., 2020; Ginski et al., 2020; Uyama et al., 2020; Jensen-Clem et al., 2020; Xie et al., 2021; Ginski et al., 2021; Hunziker et al., 2021; Ren et al., 2021; Romero et al., 2021). The developed calibration and data-reduction methods can also be applied to other current and future high-contrast imaging polarimeters, including those on the future extremely large telescopes.

Chapter 3: Calibration of the instrumental polarization effects of SCExAO-CHARIS

In Chapter 3 we present the preliminary results of the characterization of the instrumental polarization effects of the low-resolution spectropolarimetric mode of SCExAO-CHARIS. Similar to Chapter 2, we performed measurements with the internal light source and find that the image derotator produces strong wavelength-dependent crosstalk that can cause significant loss of signal. We calculate the IP, which is almost entirely produced by the telescope, using theoretical models. To complete the calibrations, we plan to measure the IP of the telescope with observations of an unpolarized star and add a data-reduction method that corrects for the instrumental polarization effects to the existing CHARIS post-processing pipeline. Once finished, the calibrations of the spectropolarimetric mode of CHARIS will enable unique quantitative polarimetric studies of circumstellar disks and substellar companions at a spectral resolution beyond that possible with SPHERE-IRDIS' broadband filters.

Chapter 4: Combining polarimetry and ADI for the characterization of substellar companions

In Chapter 4 we introduce an observing scheme that combines high-contrast imaging polarimetry with ADI to reach the polarimetric sensitivity required to characterize substellar companions that are located at small angular separations from their stars. To enable this technique for SPHERE-IRDIS, we have implemented pupil-tracking for IRDIS' polarimetric mode. We develop the corresponding observing strategies and data-reduction approaches, including the correction of the instrumental polarization effects as described in Chapter 2. Using this novel technique, we observed the planets of HR 8799 and the substellar companion PZ Tel B. Although we do not detect NIR polarization from these companions, we reach a polarimetric contrast of $\sim 10^{-7}$ with respect to the star, close to the photon-noise limit. We estimate the 1σ upper limits on the degree of linear polarization to be $\sim 1\%$ for the planets of HR 8799 and $\sim 0.1\%$ for PZ Tel B. The achieved polarimetric sensitivity and sub-percent polarimetric accuracy show that our technique enables the characterization of faint substellar companions located close to their stars.

Chapter 5: First detections of linear polarization from self-luminous substellar companions

In Chapter 5 we use SPHERE-IRDIS to measure the NIR linear polarization of 20 known, directly imaged, self-luminous exoplanets and brown dwarf companions. We reduce the

data using IRDAP (Chapter 2) and retrieve the polarization of the companions using aperture photometry, ADI (Chapter 4), and PSF fitting. We detect polarization signals of several tenths of a percent for DH Tau B and GSC 6214-210 B in H-band. Because these companions have previously measured hydrogen emission lines and red colors, the polarization most likely originates from spatially unresolved circumsubstellar disks. Through radiative transfer modeling, we constrain the position angles of the disks and find that the disks must have high inclinations. For the 18 other companions, we do not detect significant polarization and place subpercent upper limits on their degree of polarization. We also present images of several circumstellar disks, including that of DH Tau. The presence of the disks around DH Tau B and GSC 6214-210 B as well as the misalignment of the disk of DH Tau B with the disk around its host star suggest in-situ formation of the companions. The non-detections of polarization for the other companions may indicate the absence of circumsubstellar disks, a slow rotation rate of young companions, the upper atmospheres containing primarily submicron-sized dust grains, and/or limited cloud inhomogeneity.

The detections of the polarization of DH Tau B and GSC 6214-210 B constitute the first direct detections of polarization from substellar companions. As such, the detections show that the small polarization signals of companions can indeed be detected through high-contrast imaging polarimetry. In addition, our work demonstrates that polarimetry can be used to characterize substellar companions, revealing properties that cannot be deduced through photometry and spectroscopy alone. Finally, the observing strategies, data-reduction methods, and analysis techniques we developed can be used for future NIR polarimetric observations of companions and the search for exoplanets in reflected, polarized light.

Chapter 6: Development of a circular-polarimetric mode for SPHERE-IRDIS

In Chapter 6 we develop the observing scheme, data-reduction methods, and analysis tools to measure NIR circular polarization with SPHERE-IRDIS. We devised an observing scheme that uses the image derotator, which acts as an almost perfect quarter-wave retarder in the H- and K_s-bands (Chapter 2), as a polarization modulator to convert incident circular polarization into measurable linear polarization. We tested the technique with observations of the red hypergiant VY CMa and its surrounding nebula and reduce the data using an adapted version of IRDAP (Chapter 2). We find that the polarimetric accuracy of our measurements is limited by the linear-to-circular crosstalk that is not well calibrated. To more accurately constrain this crosstalk, we use the spatial variation of the linear polarization around VY CMa to distinguish between real, astrophysical circular polarization and crosstalk-induced signal. We find that the light from VY CMa is circularly polarized, in agreement with the literature, but do not conclusively detect spatially resolved circular polarization in the nebula surrounding VY CMa.

The seeing-limited instruments that have so far been used to measure NIR circular polarization cannot reach the high contrast and subarcsecond resolution required to image protoplanetary disks and the nebulae surrounding evolved stars. Our observing scheme therefore enables the first measurements of spatially resolved NIR circular polarization in these systems. Such measurements can yield strong constraints on the distribution of

the scattering material, dust properties, and magnetic-field geometries. In the case of protoplanetary disks, measurements of NIR circular polarization could even shed light on the emergence of homochirality in biomolecules.

Chapter 7: Investigation of polarization-dependent beam shifts in high-contrast imagers and telescopes

In Chapter 7 we investigate polarization aberrations produced by reflection off flat metallic mirrors at the fundamental level. Polarization aberrations are typically modeled with numerical codes, but these codes provide little insight into the full range of effects, their origin, and possible ways to mitigate them. We use polarization ray tracing to numerically compute polarization aberrations and interpret the results in terms of the polarization-dependent spatial and angular Goos-Hänchen and Imbert-Federov shifts of the beam of light as described in the physics literature. We find that all four beam shifts are fully reproduced by polarization ray tracing. We study the origin of the shifts as well as the dependence of their size and direction on the beam intensity profile, incident polarization state, angle of incidence, mirror material, and wavelength. Of the four beam shifts, only the spatial Goos-Hänchen and Imbert-Federov shifts are relevant because they are visible in the focal plane and create polarization structure in the PSF that reduces the performance of coronagraphs and the polarimetric speckle suppression close to the star. The beam shifts in an optical system can be mitigated by keeping the f-numbers large and angles of incidence small as well as by designing mirror coatings to have a retardance close to 180° rather than maximum reflectivity. Our insights can be applied to improve the performance of SPHERE-ZIMPOL and future space- and ground-based high-contrast imagers that aim to reach the extreme contrasts required to directly image exoplanets in reflected, polarized light.

1.5 Outlook

By calibrating the instrumental polarization effects of high-contrast imaging polarimeters with a polarimetric accuracy of $\lesssim 0.1\%$ in the degree of linear polarization, we can now accurately determine the linearly polarized intensity and angle of linear polarization of protoplanetary disks and debris disks. By comparing these observations with accurate radiative transfer models, we can determine the properties of the scattering dust grains. To further characterize the dust grains, the next step is to routinely and accurately determine the degree of linear polarization of disks. For this we need to obtain an image of the disk in total intensity. This is challenging, however, and large uncertainties in the disk's total intensity remain after subtracting the stellar PSF using current methods (such as ADI), thus strongly limiting the accuracy with which we can determine the degree of linear polarization (e.g., Perrin et al., 2015; Hunziker et al., 2021). To routinely measure the degree of linear polarization, we therefore need significant advances in observing strategies and data-reduction techniques (e.g., Wahhaj et al., 2021).

To enable the full characterization of circumstellar disks and the comparison with more refined radiative transfer models, we should work toward enabling full-Stokes, high-

resolution spectropolarimetry on high-contrast imagers. As a first step, we should measure the broadband circular polarization of disks, for which we could add quarter-wave plates to the current instruments. In addition, we should perform spectropolarimetry of disks, initially at low spectral resolution with, for example, SCExAO-CHARIS, and later with higher resolution by, for example, combining the long-slit spectroscopy mode of SPHERE-IRDIS with polarimetry. The latter mode could also enable the measurement of the distribution and abundance of water ice in disks (Clark et al., 2014), which can yield key information on the formation of planets and the delivery of water to rocky exoplanets (e.g., Morbidelli et al., 2000; Kobayashi et al., 2008; D'Angelo et al., 2010; Gundlach & Blum, 2015). All the efforts to characterize circumstellar disks will be aided by future improvements to the current high-contrast imagers, such as those proposed with SPHERE+ (Boccaletti et al., 2020b), GPI 2.0 (Chilcote et al., 2018), and SCExAO (Lozi et al., 2020b).

We have shown that we can measure the NIR linear polarization originating from spatially unresolved disks around young substellar companions. The next step is to detect the polarization signals due to dust scattering in the atmospheres of self-luminous companions. To detect these signals, we most likely need to reach a polarimetric accuracy of <0.01% in the degree of linear polarization, almost an order of magnitude better than the accuracy we attained with SPHERE-IRDIS. Although such a high accuracy is challenging, it has been achieved by Millar-Blanchaer et al. (2020) with their (non-high-contrast) polarimetric measurements of the brown-dwarf binary Luhman 16 using NACO at the Very Large Telescope. The authors could reach this accuracy because they kept the entire instrument at a fixed orientation with respect to the telescope during the observations, thereby stabilizing the instrumental polarization effects. Of the current high-contrast imaging polarimeters, GPI is the only instrument with a similarly stable configuration and may therefore be the most likely instrument to reach the polarimetric accuracy required to detect polarization due to dust scattering in companion atmospheres.

SPHERE-ZIMPOL has so far not been able to detect the reflected, polarized visible light of giant exoplanets (Hunziker et al., 2020). Part of the reason for these non-detections may be polarization aberrations, because the polarimetric speckle suppression of the instrument at small angular separations is limited by polarization-dependent beam shifts (Schmid et al., 2018). We should therefore measure and characterize these beam shifts so that we can devise an observing strategy that minimizes the effect of the beam shifts or can develop a method to accurately correct the shifts in the data reduction. However, it is still unclear whether SPHERE-ZIMPOL can reach a sufficiently high polarimetric sensitivity to detect giant exoplanets after the beam-shift artifacts are mitigated.

During the design of the current high-contrast imagers, polarimetry was often an afterthought and, as a result, the polarimetric sensitivity and accuracy of the instruments are not optimal. To be able to detect rocky exoplanets in reflected, polarized light with future high-contrast imagers, the polarimetric performance should be considered from the start of the design. The design process should particularly focus on minimizing polarization aberrations; instrumental polarization effects can be calibrated with sufficient accuracy and are therefore only of secondary importance. Only by controlling and mitigating the polarization aberrations can future high-contrast imagers and space telescopes such as PCS (or EPICS), PSI, HabEx, and LUVOIR reach the extreme contrasts of 10^{-8}–10^{-10}.

With these instruments and telescopes we may then be able to detect and characterize rocky exoplanets, determine their habitability, and perhaps answer the question whether there is life beyond Earth.

References

Amara, A., & Quanz, S. P. 2012, Monthly Notices of the Royal Astronomical Society, 427, 948
Bagnulo, S., Landolfi, M., Landstreet, J., et al. 2009, Publications of the Astronomical Society of the Pacific, 121, 993
Bailey, J. 2007, Astrobiology, 7, 320
Bailey, V. P., Bottom, M., Cady, E., et al. 2018, in Space Telescopes and Instrumentation 2018: Optical, Infrared, and Millimeter Wave, Vol. 10698, International Society for Optics and Photonics, 106986P
Baraffe, I., Chabrier, G., Barman, T., Allard, F., & Hauschildt, P. 2003, Astronomy & Astrophysics, 402, 701
Bastien, P., & Menard, F. 1990, Astrophysical Journal, 364, 232
Bate, M. R. 1998, Astrophysical Journal Letters, 508, L95
—. 2009, Monthly Notices of the Royal Astronomical Society, 392, 590
Beckwith, S. V., & Sargent, A. I. 1996, Nature, 383, 139
Benisty, M., Juhasz, A., Boccaletti, A., et al. 2015, Astronomy & Astrophysics, 578, L6
Benisty, M., Stolker, T., Pohl, A., et al. 2017, Astronomy & Astrophysics, 597, A42
Beuzit, J.-L., Vigan, A., Mouillet, D., et al. 2019, Astronomy & Astrophysics, 631, A155
Bhowmik, T., Boccaletti, A., Thébault, P., et al. 2019, Astronomy & Astrophysics, 630, A85
Boccaletti, A., Di Folco, E., Pantin, E., et al. 2020a, Astronomy & Astrophysics, 637, L5
Boccaletti, A., Chauvin, G., Mouillet, D., et al. 2020b, arXiv preprint arXiv:2003.05714
Bodenheimer, P., D'Angelo, G., Lissauer, J. J., Fortney, J. J., & Saumon, D. 2013, Astrophysical Journal, 770, 120
Bonnefoy, M., Zurlo, A., Baudino, J.-L., et al. 2016, Astronomy & Astrophysics, 587, A58
Boss, A. P. 1997, Science, 276, 1836
Bouvier, J., Chelli, A., Allain, S., et al. 1999, Astronomy and Astrophysics, 349, 619
Bowler, B. P. 2016, Publications of the Astronomical Society of the Pacific, 128, 102001
Bowler, B. P., Liu, M. C., Kraus, A. L., & Mann, A. W. 2014, Astrophysical Journal, 784, 65
Breckinridge, J. B., Lam, W. S. T., & Chipman, R. A. 2015, Publications of the Astronomical Society of the Pacific, 127, 445
Buenzli, E., & Schmid, H. M. 2009, Astronomy & Astrophysics, 504, 259
Cameron, A. 1978, The Moon and the Planets, 18, 5
Canovas, H., Rodenhuis, M., Jeffers, S., Min, M., & Keller, C. 2011, Astronomy & Astrophysics, 531, A102
Canovas, H., Montesinos, B., Schreiber, M., et al. 2018, Astronomy & Astrophysics, 610, A13
Canup, R. M., & Ward, W. R. 2002, The Astronomical Journal, 124, 3404
Chabrier, G., Baraffe, I., Allard, F., & Hauschildt, P. 2000, Astrophysical Journal, 542, 464
Chambers, J. E. 2004, Earth and Planetary Science Letters, 223, 241
Chilcote, J. K., Bailey, V. P., De Rosa, R., et al. 2018, in Ground-based and Airborne Instrumentation for Astronomy VII, Vol. 10702, International Society for Optics and Photonics, 1070244
Chipman, R. A. 1989, Optical engineering, 28, 280290
Clark, R. N., Swayze, G. A., Carlson, R., Grundy, W., & Noll, K. 2014, Reviews in Mineralogy and Geochemistry, 78, 399
D'Angelo, G., Durisen, R. H., & Lissauer, J. J. 2010, Exoplanets, 319

de Boer, J., Girard, J. H., Mawet, D., et al. 2014, in Ground-based and Airborne Instrumentation for Astronomy V, Vol. 9147, International Society for Optics and Photonics, 914787
de Boer, J., Salter, G., Benisty, M., et al. 2016, Astronomy & Astrophysics, 595, A114
de Boer, J., Langlois, M., van Holstein, R. G., et al. 2020, Astronomy & Astrophysics, 633, A63
de Kok, R., Stam, D., & Karalidi, T. 2011, Astrophysical Journal, 741, 59
Dohlen, K., Langlois, M., Saisse, M., et al. 2008, in Ground-based and Airborne Instrumentation for Astronomy II, Vol. 7014, International Society for Optics and Photonics, 70143L
Dong, R., Fung, J., & Chiang, E. 2016, Astrophysical Journal, 826, 75
Dong, R., Zhu, Z., Rafikov, R. R., & Stone, J. M. 2015, Astrophysical Journal Letters, 809, L5
Engler, N., Schmid, H. M., Thalmann, C., et al. 2017, Astronomy & Astrophysics, 607, A90
Esposito, T. M., Kalas, P., Fitzgerald, M. P., et al. 2020, The Astronomical Journal, 160, 24
Fitzgerald, M., Bailey, V., Baranec, C., et al. 2019, Bulletin of the American Astronomical Society, 51, 251
Fried, D. L. 1966, Journal of the Optical Society of America, 56, 1372
Garufi, A., Benisty, M., Pinilla, P., et al. 2018, Astronomy & Astrophysics, 620, A94
Garufi, A., Avenhaus, H., Pérez, S., et al. 2020, Astronomy & Astrophysics, 633, A82
Gaudi, B. S., Seager, S., Mennesson, B., et al. 2020, arXiv preprint arXiv:2001.06683
Ginski, C., Stolker, T., Pinilla, P., et al. 2016, Astronomy & Astrophysics, 595, A112
Ginski, C., Benisty, M., van Holstein, R., et al. 2018, Astronomy & Astrophysics, 616, A79
Ginski, C., Ménard, F., Rab, C., et al. 2020, Astronomy & Astrophysics, 642, A119
Ginski, C., Facchini, S., Huang, J., et al. 2021, Astrophysical Journal Letters, 908, L25
Gledhill, T., & McCall, A. 2000, Monthly Notices of the Royal Astronomical Society, 314, 123
Greenwood, D. P. 1977, Journal of the Optical Society of America, 67, 390
Grinin, V. 2000, in Disks, Planetesimals, and Planets, Vol. 219, 216
Groff, T., Chilcote, J., Brandt, T., et al. 2017, in Techniques and Instrumentation for Detection of Exoplanets VIII, Vol. 10400, International Society for Optics and Photonics, 1040016
Gundlach, B., & Blum, J. 2015, Astrophysical Journal, 798, 34
Guyon, O. 2018, Annual Review of Astronomy and Astrophysics, 56, 315
Guyon, O., Pluzhnik, E., Kuchner, M. J., Collins, B., & Ridgway, S. 2006, Astrophysical Journal Supplement Series, 167, 81
Hamaker, J., & Bregman, J. 1996, Astronomy and Astrophysics Supplement Series, 117, 161
Hennebelle, P., & Chabrier, G. 2008, Astrophysical Journal, 684, 395
Hollenbach, D. J., Yorke, H. W., & Johnstone, D. 2000, Protostars and planets IV, 401, 12
Hunziker, S., Schmid, H. M., Mouillet, D., et al. 2020, Astronomy & Astrophysics, 634, A69
Hunziker, S., Schmid, H., Ma, J., et al. 2021, Astronomy & Astrophysics, 648, A110
Jensen-Clem, R., Millar-Blanchaer, M., Mawet, D., et al. 2016, Astrophysical Journal, 820, 111
Jensen-Clem, R., Millar-Blanchaer, M. A., van Holstein, R. G., et al. 2020, The Astronomical Journal, 160, 286
Jovanovic, N., Martinache, F., Guyon, O., et al. 2015, Publications of the Astronomical Society of the Pacific, 127, 890
Karalidi, T., & Stam, D. 2012, Astronomy & Astrophysics, 546, A56
Karalidi, T., Stam, D., & Hovenier, J. 2011, Astronomy & Astrophysics, 530, A69
—. 2012, Astronomy & Astrophysics, 548, A90
Kasdin, N. J., Bailey, V., Mennesson, B., et al. 2020, in Space Telescopes and Instrumentation 2020: Optical, Infrared, and Millimeter Wave, Vol. 11443, International Society for Optics and Photonics, 114431U
Kasper, M., Urra, N. C., Pathak, P., et al. 2020, Messenger (182)
Keller, C. U. 2002, Astrophysical Spectropolarimetry, 1, 303
Kennedy, G. M., Ginski, C., Kenworthy, M. A., et al. 2020, Monthly Notices of the Royal Astro-

nomical Society: Letters, 496, L75
Keppler, M., Benisty, M., Müller, A., et al. 2018, Astronomy & Astrophysics, 617, A44
Keppler, M., Penzlin, A., Benisty, M., et al. 2020, Astronomy & Astrophysics, 639, A62
Kley, W., & Nelson, R. 2012, Annual Review of Astronomy and Astrophysics, 50, 211
Kobayashi, H., Watanabe, S.-i., Kimura, H., & Yamamoto, T. 2008, Icarus, 195, 871
Kratter, K. M., Murray-Clay, R. A., & Youdin, A. N. 2010, Astrophysical Journal, 710, 1375
Kraus, S., Kreplin, A., Young, A. K., et al. 2020, Science, 369, 1233
Kuhn, J., Potter, D., & Parise, B. 2001, Astrophysical Journal Letters, 553, L189
Langlois, M., Gratton, R., Lagrange, A.-M., et al. 2021, Astronomy & Astrophysics, 651, A71
Larkin, J. E., Chilcote, J. K., Aliado, T., et al. 2014, in Ground-based and Airborne Instrumentation for Astronomy V, Vol. 9147, International Society for Optics and Photonics, 91471K
Lozi, J., Guyon, O., Kudo, T., et al. 2020a, in Adaptive Optics Systems VII, Vol. 11448, International Society for Optics and Photonics, 114487C
Lozi, J., Guyon, O., Vievard, S., et al. 2020b, in Adaptive Optics Systems VII, Vol. 11448, International Society for Optics and Photonics, 114480N
LUVOIR Team. 2019, arXiv preprint arXiv:1912.06219
Lyot, B. 1939, Monthly Notices of the Royal Astronomical Society, 99, 580
Macintosh, B., Graham, J. R., Ingraham, P., et al. 2014, Proceedings of the National Academy of Sciences, 111, 12661
Marley, M. S., & Sengupta, S. 2011, Monthly Notices of the Royal Astronomical Society, 417, 2874
Marois, C., Lafreniere, D., Doyon, R., Macintosh, B., & Nadeau, D. 2006, Astrophysical Journal, 641, 556
Mawet, D., Pueyo, L., Lawson, P., et al. 2012, in Space Telescopes and Instrumentation 2012: Optical, Infrared, and Millimeter Wave, Vol. 8442, International Society for Optics and Photonics, 844204
McGuire, J. P., & Chipman, R. A. 1990, Journal of the Optical Society of America A, 7, 1614
—. 1994a, Applied optics, 33, 5080
—. 1994b, Applied optics, 33, 5101
McKee, C. F., & Ostriker, E. C. 2007, Annual Review of Astronomy and Astrophysics, 45, 565
Menard, F., Bouvier, J., Dougados, C., Mel'nikov, S. Y., & Grankin, K. N. 2003, Astronomy & Astrophysics, 409, 163
Ménard, F., Cuello, N., Ginski, C., et al. 2020, Astronomy & Astrophysics, 639, L1
Millar-Blanchaer, M. A., Graham, J. R., Pueyo, L., et al. 2015, Astrophysical Journal, 811, 18
Millar-Blanchaer, M. A., Perrin, M. D., Hung, L.-W., et al. 2016, in Ground-based and Airborne Instrumentation for Astronomy VI, Vol. 9908, International Society for Optics and Photonics, 990836
Millar-Blanchaer, M. A., Girard, J. H., Karalidi, T., et al. 2020, Astrophysical Journal, 894, 42
Milli, J., Mawet, D., Pinte, C., et al. 2015, Astronomy & Astrophysics, 577, A57
Morbidelli, A., Chambers, J., Lunine, J., et al. 2000, Meteoritics & Planetary Science, 35, 1309
Müller, A., Keppler, M., Henning, T., et al. 2018, Astronomy & Astrophysics, 617, L2
Muro-Arena, G. A., Ginski, C., Dominik, C., et al. 2020, Astronomy & Astrophysics, 636, L4
Muto, T., Grady, C., Hashimoto, J., et al. 2012, Astrophysical Journal Letters, 748, L22
Nakamoto, T., & Nakagawa, Y. 1994, Astrophysical Journal, 421, 640
Nielsen, E. L., De Rosa, R. J., Macintosh, B., et al. 2019, The Astronomical Journal, 158, 13
Olofsson, J., Samland, M., Avenhaus, H., et al. 2016, Astronomy & Astrophysics, 591, A108
Olofsson, J., van Holstein, R. G., Boccaletti, A., et al. 2018, Astronomy & Astrophysics, 617, A109
Olofsson, J., Milli, J., Thébault, P., et al. 2019, Astronomy & Astrophysics, 630, A142
Patty, C. L., Ten Kate, I. L., Buma, W. J., et al. 2019, Astrobiology, 19, 1221
Perrin, M. D., Duchene, G., Millar-Blanchaer, M., et al. 2015, Astrophysical Journal, 799, 182

Pinilla, P., Benisty, M., de Boer, J., et al. 2018, Astrophysical Journal, 868, 85
Pohl, A., Sissa, E., Langlois, M., et al. 2017, Astronomy & Astrophysics, 605, A34
Pollack, J. B., Hubickyj, O., Bodenheimer, P., et al. 1996, Icarus, 124, 62
Quanz, S. P., Avenhaus, H., Buenzli, E., et al. 2013, Astrophysical Journal Letters, 766, L2
Ren, B., Dong, R., van Holstein, R. G., et al. 2020, Astrophysical Journal Letters, 898, L38
Ren, B., Choquet, É., Perrin, M. D., et al. 2021, Astrophysical Journal, 914, 95
Rigliaco, E., Gratton, R., Kóspál, Á., et al. 2020, Astronomy & Astrophysics, 641, A33
Romero, C., Milli, J., Lagrange, A. M., et al. 2021, Astronomy & Astrophysics, 651, A34
Rossi, L., & Stam, D. 2017, Astronomy & Astrophysics, 607, A57
Rossi, L., & Stam, D. M. 2018, Astronomy & Astrophysics, 616, A117
Rostopchina, A., Grinin, V., Okazaki, A., et al. 1997, Astronomy and Astrophysics, 327, 145
Ruane, G., Riggs, A., Mazoyer, J., et al. 2018, in Space Telescopes and Instrumentation 2018: Optical, Infrared, and Millimeter Wave, Vol. 10698, International Society for Optics and Photonics, 106982S
Sanchez Almeida, J., & Martinez Pillet, V. 1992, Astronomy and Astrophysics, 260, 543
Schmid, H. M., Bazzon, A., Roelfsema, R., et al. 2018, Astronomy & Astrophysics, 619, A9
Sengupta, S., & Krishan, V. 2001, Astrophysical Journal Letters, 561, L123
Sengupta, S., & Marley, M. S. 2010, Astrophysical Journal Letters, 722, L142
Shu, F. H. 1977, Astrophysical Journal, 214, 488
Shu, F. H., Adams, F. C., & Lizano, S. 1987, Annual Review of Astronomy and Astrophysics, 25, 23
Snik, F., & Keller, C. U. 2013, Planets, Stars and Stellar Systems, 2, 175
Soummer, R., Pueyo, L., & Larkin, J. 2012, Astrophysical Journal Letters, 755, L28
Sparks, W., Hough, J., Kolokolova, L., et al. 2009, Journal of Quantitative Spectroscopy and Radiative Transfer, 110, 1771
Spergel, D., Gehrels, N., Baltay, C., et al. 2015, arXiv preprint arXiv:1503.03757
Stam, D. 2008, Astronomy & Astrophysics, 482, 989
Stam, D., Hovenier, J., & Waters, L. 2004, Astronomy & Astrophysics, 428, 663
Stamatellos, D., Hubber, D. A., & Whitworth, A. P. 2007, Monthly Notices of the Royal Astronomical Society: Letters, 382, L30
Stamatellos, D., & Whitworth, A. P. 2009, Monthly Notices of the Royal Astronomical Society, 392, 413
Stolker, T., Dominik, C., Min, M., et al. 2016a, Astronomy & Astrophysics, 596, A70
Stolker, T., Min, M., Stam, D. M., et al. 2017, Astronomy & Astrophysics, 607, A42
Stolker, T., Dominik, C., Avenhaus, H., et al. 2016b, Astronomy & Astrophysics, 595, A113
Szulágyi, J., Mayer, L., & Quinn, T. 2017, Monthly Notices of the Royal Astronomical Society, 464, 3158
Tinbergen, J. 2005, Astronomical polarimetry (Cambridge University Press)
Traub, W. A., & Oppenheimer, B. R. 2010, Direct imaging of exoplanets (University of Arizona Press, Tucson)
Trees, V. J., & Stam, D. M. 2019, Astronomy & Astrophysics, 626, A129
Uyama, T., Ren, B., Mawet, D., et al. 2020, The Astronomical Journal, 160, 283
Van Boekel, R., Henning, T., Menu, J., et al. 2017, Astrophysical Journal, 837, 132
Vigan, A., Langlois, M., Moutou, C., & Dohlen, K. 2008, Astronomy & Astrophysics, 489, 1345
Wahhaj, Z., Milli, J., Romero, C., et al. 2021, Astronomy & Astrophysics, 648, A26
Wiktorowicz, S. J., Millar-Blanchaer, M., Perrin, M. D., et al. 2014, in Ground-based and Airborne Instrumentation for Astronomy V, Vol. 9147, International Society for Optics and Photonics, 914783
Williams, D. M., & Gaidos, E. 2008, Icarus, 195, 927

Williams, J. P., & Cieza, L. A. 2011, Annual Review of Astronomy and Astrophysics, 49, 67
Witzel, G., Eckart, A., Buchholz, R., et al. 2011, Astronomy & Astrophysics, 525, A130
Wyatt, M. C. 2008, Annual Review of Astronomy and Astrophysics, 46, 339
Xie, C., Ren, B., Dong, R., et al. 2021, Astrophysical Journal Letters, 906, L9
Yorke, H. W., Bodenheimer, P., & Laughlin, G. 1993, Astrophysical Journal, 411, 274
Zhu, Z., Dong, R., Stone, J. M., & Rafikov, R. R. 2015, Astrophysical Journal, 813, 88